ELSEVIER

CrossMark

Microstructural effects on the average properties in porous battery electrodes

Ramiro García-García [b], R. Edwin García [a],[*]

[a] *School of Materials Engineering, Purdue University, USA*
[b] *Instituto de Física, UNAM, Apdo. Postal 20/364, 01000 D.F., Mexico*

HIGHLIGHTS

- Developed model to predict generalized tortuosity- and reactity−porosity relations.
- Through-thickness Bruggeman exponent increases for plate-like particles.
- For aligned particles tortuosity is dramatically suppressed in needle-shaped particles.
- Electrode area density can be tuned as the particles become increasingly oblate.
- Electrode area density reaches a minimum as particles become increasingly prolate.

ARTICLE INFO

ABSTRACT

A theoretical framework is formulated to analytically quantify the effects of the microstructure on the average properties of porous electrodes, including reactive area density and the through-thickness tortuosity as observed in experimentally-determined tomographic sections. The proposed formulation includes the microstructural non-idealities but also captures the well-known perfectly spherical limit. Results demonstrate that in the absence of any particle alignment, the through-thickness Bruggeman exponent α, reaches an asymptotic value of $\alpha \sim 2/3$ as the shape of the particles become increasingly prolate (needle- or fiber-like). In contrast, the Bruggeman exponent diverges as the shape of the particles become increasingly oblate, regardless of the degree of particle alignment. For aligned particles, tortuosity can be dramatically suppressed, *e.g.*, $\alpha \rightarrow 1/10$ for $r_a \rightarrow 1/10$ and $MRD \sim 40$. Particle size polydispersity impacts the porosity-tortuosity relation when the average particle size is comparable to the thickness of the electrode layers. Electrode reactivity density can be arbitrarily increased as the particles become increasingly oblate, but asymptotically reach a minimum value as the particles become increasingly prolate. In the limit of a porous electrode comprised of fiber-like particles, the area density decreases by 24%, with respect to a distribution of perfectly spherical particles.

© 2015 Elsevier B.V. All rights reserved.

1. Introduction

The successful commercialization of advanced rechargeable batteries is directly linked to the ability to manufacture porous electrochemical architectures that balance performance, long term reliability, and price [1,2]. Today, affordable porous battery electrodes are produced by integrating a slurry comprised of active material, binders, and conductive phases into a tape cast layer that has been carefully dried, pressed, and infiltrated with a liquid electrolyte [3]. The resultant granular microstructure (see Fig. 1) aims to strike a balance between delivering a high reactive area density per unit volume at the expense of sacrificing precious energy density, or delivering a large volume of particles of active material at the expense of sacrificing power density. Fundamentally, this dichotomy is a result of the suboptimal packing of a random distribution of particles of active material into random jammed states where the asphericity of the granules determines not only the likelihood of statistically realizable packed configurations, but the resultant through-thickness tortuosity and the mean reactive area density.

Historically, the tortuosity has been correlated to the macroscopic conductivity, σ_T through the relation,
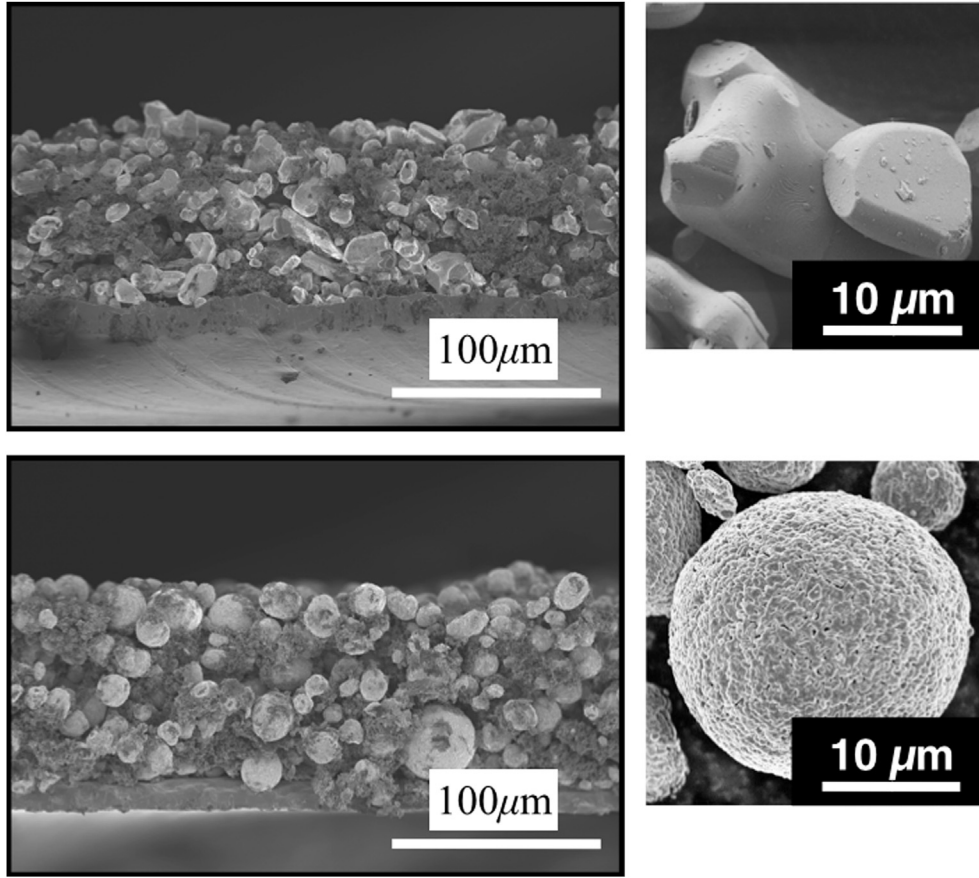
Fig. 1. Two microstrostructurally similar porous positive electrode layers of comparable porosities and average particle size. However, the characteristic morphology of the LCO layer (top two insets) induces a greater amount of tortuosity and lower reactivity per unit area as compared to the NMC layer (bottom two insets), which delivers microstructural tortuosities and reactivities much closer to the Bruggeman ideal, as reported by Chung, Ebner, Wood, and García [8].

$$\sigma_T = \sigma_1 \frac{\varepsilon}{\tau} \tag{1}$$

where σ_1 is the conductivity of the electrolyte matrix, ε is the porosity of the composite electrode, and

$$\tau = \frac{1}{\varepsilon^\alpha} \tag{2}$$

is the generalized Bruggeman porosity-tortuosity relationship. In Equation (2), α is the generalized Bruggeman exponent [5]. τ embodies the spatial weighted average contributions to the deviations from a perfectly homogeneous medium by the random distribution of particles of active material. In the past sixty years, the classic Bruggeman relation, $\tau = 1/\varepsilon^{1/2}$ ($\alpha = 1/2$) [5], has been widely used by the battery community to parameterize material properties in Newman-type (microstructurally averaged) models, based on the very successful porous electrode theory by assuming a uniform spatial distribution of perfectly spherical monodispersed particles [4]. Most recently, these coefficients have been empirically adapted to describe non-ideal situations, *i.e.*, $\alpha \neq 1/2$ values, without establishing a rational connection to its underlying components, particle morphology, or processing-microstructural correlations. Recently published efforts have highlighted the effect of asphericity on the classic and the generalized Bruggeman exponent, *e.g.*, Thorat and Wheeler [6], Shearing, Harris, et al. [7], Chung and García [8,9] Ebner, Chung et al. [10], and others [11,12]. In all these efforts,

experimentally determined CT-scans and computer-generated three-dimensional representations of porous electrode microstructures have been combined as a means to directly establish correlations between processing, microstructure, and electrochemical properties. These analyses have demonstrated that the spatial inhomogeneities that develop in commercial battery electrodes [6−10,13−15], enable the identification of important microstructural features such as particle clustering [7,8], to verify and quantify processing-induced tortuosity anisotropy relations [10,15], and as a starting point to formulate semi-analytical [16], and analytical porosity-tortuosity descriptions, by using contributions from the individual meso- and microscale phases [15].

In contrast, the reactivity of an electrode layer has been historically determined by directly quantifying the area per unit volume, $\mathscr{A}$, of a monodispersed distribution of perfectly spherical particles, *i.e.* [17,18],

$$
\begin{aligned}
\mathscr{A} &= \frac{4\pi r_p^2}{\frac{4}{3}\pi r_p^3}(1-\varepsilon) \\
&= \frac{3}{r_p}(1-\varepsilon)
\end{aligned}
\tag{3}
$$

where r_p is the microstructurally representative radius of the particles. Chung et al. [9], has improved on this description by using CT sections and discrete element model calculations to show that the

reactivity of experimental sections deviates up to a factor of three by simply including the effect of particle size polydispersity, and off by a factor of five by incorporating the effect of surface roughness. These results were summarized into generalized expressions of the form:

$$\mathscr{A} = \frac{\mathscr{K}}{r_p}(1 - \varepsilon) \tag{4}$$

where $\mathscr{K}$ embodies to the microstructural contributions to polydispersity and particle roughness of the electrode layer.

Overall, the microstructural characteristics imposed by the battery fabrication process define physical properties that will ultimately control the instantaneous performance and the long term reliability of the porous energy storage device. These material descriptions are routinely incorporated into empirical constitutive relations that enter Newman-type models to help rationalize and thus design the charge transport across the through-thickness of the rocking chair device, making it critical to capture the relevant effects. In spite of its importance, a formal description that aims to include the non-idealities associated to the microstructural tortuosity and reactivity in granular structures remains unavailable. In this paper, we propose a formalism that starts from the fundamental description of individual particles to predict, abstract, and rationalize the effects of microstructural polydispersity, naturally found in commercial electrodes. The analytical framework described herein incorporates details of individual particles into statistical representations that allows to construct experimentally verifiable macroscopic properties to describe the next generation of advanced electrochemical materials.

2. Theoretical framework

2.1. Macroscopic properties in diluted systems

For a two phase porous composite of total volume $V_T = V_1 + V_2$, phase 1 is the background electrolyte of electrical conductivity σ_1 and volume V_1, and phase 2 is the spatial distribution of arbitrarily shaped particles of active material of electrical conductivity σ_2 of volume V_2. The macroscopic charge flux across the electrode is the volume averaged contributions over the entire electrode layer, $\langle J_i \rangle = \frac{1}{V_T} \int_{V_T} \sigma(\vec{x})E_i dV$, which can be divided into the spatial contributions from each individual phase:

$$\langle J_i \rangle = \frac{1}{V_T} \int_{V_1} \sigma_1 E_i dV + \frac{1}{V_T} \int_{V_2} \sigma_2 E_i dV \tag{5}$$

and rearranged to highlight the charge flux contributions from the active material volume fraction, $\phi_2 = V_2/V_T$:

$$\langle J_i \rangle = \frac{\sigma_1}{V_T} \int_{V_T} E_i dV + \frac{(\sigma_2 - \sigma_1)\phi_2}{V_2} \int_{V_2} E_i dV \tag{6}$$

and further rewritten as [19]:

$$\langle J_i \rangle = \sigma_1 \langle E_i^\circ \rangle + (\sigma_2 - \sigma_1)\phi_2 \langle E_i^p \rangle_{\text{average}} \tag{7}$$

The first term on the right side of Equation (7) embodies the contributions of the electrolyte to the total macroscopic electrical charge flux in the absence of phase 2, while the second term corresponds to the volume averaged correction to the macroscopic charge flux as a result of the individual contributions from the particles of active material, modulated by the macroscopic electric

field inside the particle phase distribution, $\langle E_i^p \rangle_{\text{average}}$, and the material properties contrast between both phases, i.e., $\Delta\sigma = \sigma_2 - \sigma_1$.

The internal electric field of an individual particle, $\langle E_i^p \rangle$, is a direct result of its specific shape, its orientation in space relative to the macroscopically applied (external) electric field, and its interactions with the immediate surrounding environment. In agreement with Giordano [20], the internal electric field of an isolated particle in the presence of an externally applied electric field, $\langle E_i^\circ \rangle$, is given by:

$$\langle E_i^p \rangle = \sum_{k=1}^{3} \sum_{j=1}^{3} \frac{n_{k,i}^E n_j \langle E_k^\circ \rangle}{1 + L_j(\sigma_2 - \sigma_1)/\sigma_1} \tag{8}$$

where L_j embodies the contributions to the morphology of the particle along the j-th direction, and is known as the depolarization factor, as introduced by Stratton and reviewed by Torquato for ellipsoidal particles [21,22]. L_j provides its lowest values in the direction of the particle that exposes its lowest cross-section (least resistance) for charge flux. n_j is the j-th component of the normalized principal direction of the particle and represents the orientation of an arbitrarily shaped inclusion with respect to a laboratory reference frame. Similarly, $n_{k,i}^E$ is the k-th component of the normalized principal direction of the externally applied (far) electric field, with respect to the i-th direction.

Physically, the particle distribution displayed by a commercial porous electrode is defined through the underlying particle−particle interactions during powder processing, electrode compaction, and calendering [3,6,10]. The resultant overall spatial particle population configuration will directly impact on the macroscopic properties of the electrode and the long term reliability of the electrochemical composite. Statistically, the resultant electrode microstructure is represented in terms of a probability density distribution, $p_T(\vec{t})$, where $\vec{t}$ is a vector of microstructural parameters that represent the relevant topological characteristics of the composite layer. Overall, $p_T(\vec{t})$ determines the total probability of finding a particle subpopulation between the microstructural parameter value $\vec{t}$ and $\vec{t} + d\vec{t}$, subjected to the constraint, $\int_{\vec{t}} p_T(\vec{t})d\vec{t} = 1$. A realistic particle probability distribution, includes a description of the orientation probability density distribution, which accounts for the texturing or statistical particle alignment that results from compacting the electrode; the particle size probability density distribution, which accounts for the average particle size and associated polydispersity of the powders that comprise the conductive composite; and the morphology probability density distribution, which accounts for the shape and its morphological anisotropy in terms of their principal axes.

In this context, Equations (7) and (8) are related by considering the individual contributions from every particle to the average internal electric field of phase 2 by the entire population of particles:

$$\langle E_i^p \rangle_{\text{average}} = \int_{\vec{t}} \langle E_i^p \rangle (\vec{t}) p_T(\vec{t})d\vec{t} \tag{9}$$

Assume that the probability distribution can be separated into independent contributions that embody measurable non-idealities including the morphology probability density distribution, $p_M(a,b,c,...)$, as a function of the morphological principal axes of the particle, e.g., a, b, c only for an ellipsoidal representation of the morphology of the particle; the orientation probability distribution, $p_O(\overleftrightarrow{R})$, as a function of the rotation matrix (orientation) of each

particle, $\overleftrightarrow{R}$, which in turn can be represented in terms of the Euler angles of the particle, e.g., $\overleftrightarrow{R} = \overleftrightarrow{R}(\theta, \beta, \gamma)$; and the characteristic size of the particle, $p_S(r_p)$, e.g., as a function of the cube root of the volume of each particle, $r_p = V_p^{1/3}$. The total probability distribution is thus decoupled into separate, independent statistical contributions:

$$p_T\left(\overleftrightarrow{R}, r_p, a, b, c\right) = p_M(a,b,c) \cdot p_O\left(\overleftrightarrow{R}\right) \cdot p_S(r_p) \tag{10}$$

The macroscopic charge flux has the functional form $\langle J_i \rangle = \langle \sigma_i^\circ \rangle \langle E_i^\circ \rangle$. For the specific case of a dilute system, substitution of Equations (8) and (9) into Equation (7) enables the direct calculation of the macroscopic electrical conductivity, $\langle \sigma_i^\circ \rangle$, as has been classically done in the literature [21,23]. The resultant expression, $\langle \sigma_i^\circ \rangle = \langle \sigma_i^\circ \rangle(\phi_2, \sigma_1, \sigma_2, \overrightarrow{t})$, provides a rigorous basis to describe a distribution of non-interacting granular aggregates as a function of the powder physical and geometrical properties, $\phi_2, \sigma_1, \sigma_2, \overrightarrow{t}$, and provides a starting point to formulate non-dilute porous electrode composites, in the absence of localized particle clustering.

2.2. Macroscopic properties in non-diluted systems

Away from perfect dilution, the continuous addition of particles (phase 2), induces each individual grain to experience the background electrical charge transport properties, σ_1, to be equal to the macroscopic response, $\sigma_1 = \langle \sigma_i^\circ \rangle$, as statistically contributed by the entirety of the spatial distribution of particles. Thus, for a spatially uniform distribution of particles, the addition of small amounts of active material, $\Delta\phi_2$, relative to the existing available volume

fraction of electrolyte, ϕ_1, i.e., $\Delta c = \Delta\phi_2/\phi_1 = \Delta\phi_2/(1-\phi_2)$, will shift the macroscopic electrical conductivity by an amount, $\Delta\langle \sigma_i^\circ \rangle$. Mathematically, this is expressed as a first order Taylor series expansion:

$$\Delta\langle \sigma_i^\circ \rangle(\phi_2, \Delta c, \sigma_2, \overrightarrow{t}) \sim \frac{\partial\langle \sigma_i^\circ \rangle(\phi_2, \sigma_1 = \langle \sigma_i^\circ \rangle, \sigma_2, \overrightarrow{t})}{\partial\phi_2}\Delta c$$

$$\Rightarrow \langle \sigma_i^\circ \rangle(\phi_2 + \Delta\phi_2, \sigma_2, \overrightarrow{t}) - \langle \sigma_i^\circ \rangle(\phi_2, \sigma_2, \overrightarrow{t})$$

$$= \frac{\partial\langle \sigma_i^\circ \rangle(\phi_2, \sigma_1 = \langle \sigma_i^\circ \rangle, \sigma_2, \overrightarrow{t})}{\partial\phi_2}\left[\frac{\Delta\phi_2}{1-\phi_2}\right] \tag{11}$$

where the term $\frac{\partial\langle \sigma_i^\circ \rangle(\phi_2, \sigma_1 = \langle \sigma_i^\circ \rangle, \sigma_2, \overrightarrow{t})}{\partial\phi_2} = F(\phi_2, \sigma_1 = \langle \sigma_i^\circ \rangle, \sigma_2, \overrightarrow{t})$, corresponds to the rate of change with respect to the volume fraction of active material of the average electrical conductivity, $\langle \sigma_i^\circ \rangle(\phi_2, \sigma_1, \sigma_2, \overrightarrow{t})$ in the dilute limit, as described at the end of Section 2.1, in the limit $\sigma_1 = \langle \sigma_i^\circ \rangle$. Equation (11) corresponds to the procedure originally proposed by Bruggeman, referred to as the Differential Effective Medium (DEM) approximation to describe the average conductivity away from the dilute limit.

In the limit of $\Delta\phi_2 \to 0$, Equation (11) leads to the general differential equation:

$$(1-\phi_2)\frac{d\langle \sigma_i^\circ \rangle}{d\phi_2} = \frac{\partial\langle \sigma_i^\circ \rangle(\phi_2, \sigma_1 = \langle \sigma_i^\circ \rangle, \sigma_2, \overrightarrow{t})}{\partial\phi_2} \tag{12}$$

whose solution requires to satisfy the conditions, $\langle \sigma_i^\circ \rangle(\phi_2 = 0) = \sigma_1$ or $\langle \sigma_i^\circ \rangle(\phi_2 = 1) = \sigma_2$.

In the following section, the theoretical framework described herein is applied to predict the impact of well-known particle distributions.

3. Application to morphologically anisotropic particles

We have recently shown through direct numerical calculations [8,9], that the statistical morphological anisotropy of the utilized particles combined with the degree of alignment of particles induced by electrode processing dominates the microstructural properties. Furthermore, Ebner [16], recently showed that two-dimensional CT sections of arbitrarily shaped particles can be abstracted into numerical microstructural probability distribution representation in terms of ellipsoids of revolution of controlled volume, aspect ratio, and specified orientation distribution. By using Equation (10), this is analytically described as:

$$p_T = \delta(a - a_\circ)\delta(c/a - c_\circ/a_\circ)p_O(\overrightarrow{t}, \theta, \beta, \gamma)p_S(r_p) \tag{13}$$

Equation (13) reduces to a well known treatment, in the case of $p_O(\overrightarrow{t}, \theta, \beta, \gamma) = p_O(\theta) = \delta(\theta)$, for perfectly aligned particles, or $p_O(\overrightarrow{t}, \theta, \beta, \gamma) = p_O(\theta) = \sin\theta$, for a random distribution of particle orientations [20].

By using Equations (8) through (12), we find:

$$(1-\phi_2)\frac{d\langle \sigma_{xx}^\circ \rangle}{d\phi_2} = \langle \sigma_{xx}^\circ \rangle(\sigma_2 - \langle \sigma_{xx}^\circ \rangle)\frac{p}{3}\left[\frac{S+2}{\langle \sigma_{xx}^\circ \rangle + L(\sigma_2 - \langle \sigma_{xx}^\circ \rangle)} + \frac{1-S}{\langle \sigma_{xx}^\circ \rangle + (1-2L)(\sigma_2 - \langle \sigma_{xx}^\circ \rangle)}\right]$$

$$(1-\phi_2)\frac{d\langle \sigma_{zz}^\circ \rangle}{d\phi_2} = \langle \sigma_{zz}^\circ \rangle(\sigma_2 - \langle \sigma_{zz}^\circ \rangle)\frac{p}{3}\left[\frac{2(1-S)}{\langle \sigma_{zz}^\circ \rangle + L(\sigma_2 - \langle \sigma_{zz}^\circ \rangle)} + \frac{2S+1}{\langle \sigma_{zz}^\circ \rangle + (1-2L)(\sigma_2 - \langle \sigma_{zz}^\circ \rangle)}\right] \tag{14}$$

where $p = \int_{h_\circ/2}^{h_c/2} p_S(r_p)dr_p$, i.e., the cumulative particle size probability distribution, in agreement with Equations (10) and (13). Here $h_\circ/2$ is the smallest particle size sampled by the porous electrode layer, e.g., the smallest size sieved into the device, and h_c is the thickness of the electrode layer. Thus, for example, if the largest particle size, $r_p^{max} \ll h_c$ then $p \sim 1$. $L = L_{xx} = L_{yy}$ and $L_{zz} = 1 - 2L$. $S = \int_0^{\pi/2}\left(\frac{3}{2}\cos^2\theta - \frac{1}{2}\right)p_O(\overrightarrow{t}, \theta)d\theta$, is the microstructural order parameter. Values of $S = 1$ correspond to perfectly ordered or aligned particles (textured), while values of $S = 0$, correspond to a completely random orientation of particles (no texture), in agreement with Giordano [20].

Because the great majority of rechargeable batteries exchange Lithium along the through-thickness direction, the remainder of the paper focuses on quantifying the effect of particle shape anisotropy and degree of alignment along the thickness of the electrode layer. However, the analysis can be straight-forwardly repeated to understand the effect on the in-plane properties.

In the limit of $\sigma_2 \ll \sigma_1$ the through-thickness macroscopic

conductivity of the electrode is:

$$\left\langle \sigma_{zz}^{\circ} \right\rangle = \sigma_1 \varepsilon^{-\frac{p}{2(L-1)} - \frac{p}{6(L-1)L} + \frac{pS}{L-1} - \frac{pS}{3L(L-1)}}$$ (15)

By using Equations (1) and (2), the through-thickness Bruggeman exponent as a function of the statistical particle geometry is:

$$\left\langle \alpha_{zz} \right\rangle = \frac{p + 2pS + 3L(p - 2pS + 2L - 2)}{6L(1 - L)}$$ (16)

Equation (16) reduces to:

$$\left\langle \alpha_{zz} \right\rangle = \frac{p - 2L}{2L}$$ (17)

for perfectly aligned particles.

In contrast, Equation (16) reduces to:

$$\left\langle \alpha_{zz} \right\rangle = p\left(\frac{1}{6L} + \frac{2}{3(1 - L)}\right) - 1$$ (18)

for randomly oriented particles. The asymptotic limits, Equations (17) and (18) are in agreement with Giordano [20], in the limit of $p \rightarrow 1$, which corresponds to a monodispersed distribution of particle sizes or for electrode layers that sample the entirety of the size population.

Equations (14)–(16) show that as long as the electrode layer samples a statistically representative through thickness population of grains, the Bruggeman exponent will reach an asymptotic, minimal value, regardless of the size or morphological polydispersity of the powders that integrate the electrode layer. Thus, for electrode layers whose thickness, h_c is comparable to the particle size, i.e., $r_p \sim h_c/2$, the Bruggeman exponent and thus the tortuosity will be larger because for very thin electrode layers, the charge flux is forced to go through the particle phase, whose contribution to the conductivity of the porous layer is very small. Similarly, when the polydispersity in the morphology probability distribution leads to particles whose mayor axis is comparable to the electrode layer thickness, i.e., $r_p \times c/a \sim h_c/2$, a great deal of through thickness variability on the Bruggeman exponent will be experienced. For example, for a Gaussian distribution of particle sizes, the apparent effect of electrode layer thickness is indistinguishable from the bulk value when the particle size is at least ten times smaller than the layer through thickness, i.e., $h_c \gg r_p$.

In the remainder of this paper assume $p \sim 1$. Fig. 2 shows the effect of the depolarization factor and the microstructural order parameter on the Bruggeman exponent. Calculations show that those morphologies that expose the widest cross-sections in the direction of the charge flux will deliver the highest Bruggeman exponents, regardless of their degree of particle alignment. In contrast, fiber- or needle-like particles highly aligned in the flux direction will lead to very low Bruggeman exponents. Untextured fiber microstructures will deliver α values greater than perfectly spherical particles. As expected, perfect spheres are impervious to microstructural alignment, and deliver the classic $\alpha = 1/2$ value. In general, Fig. 2 shows that regardless of the specific details describing the characteristic morphology of the particles of active material, particle alignment is a very powerful microstructural feature that can be used to minimize tortuosity. Specifically, the fabrication of columnar structures aligned towards the counter electrode provide an $\alpha \sim 1/10$ value for 90% alignment, e.g., see Chiang et al. [24,25]. However, a microstructural order parameter of $S > 0.25$ is necessary in order for fiber-shaped particles to deliver a Bruggeman exponent smaller than that observed in perfectly spherical particles.

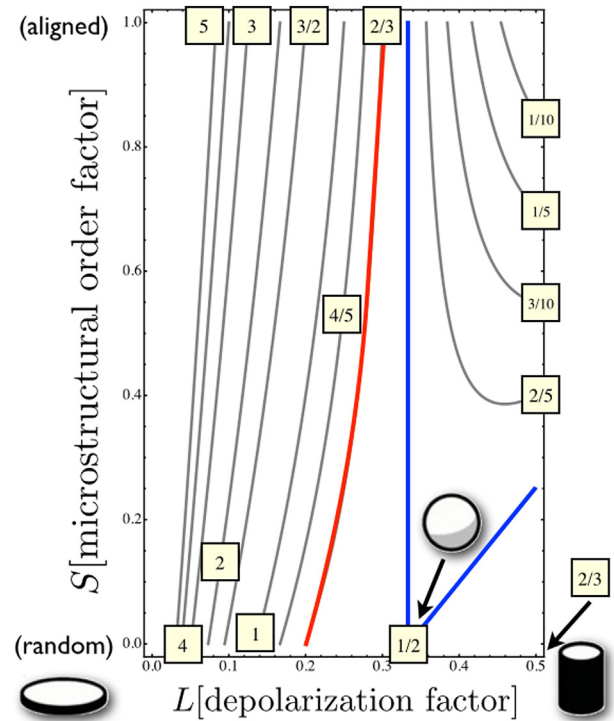For the specific case of a mixture of particles that can be

Fig. 2. Through-thickness Bruggeman exponent isocontour map as a function of geometrical depolarization factor, L, and the microstructural order parameter, S. $\alpha = 1/2$, traditionally used to describe spherical particles, is highlighted in blue. Similarly, $\alpha = 2/3$, describing the limit of no alignment for fiber textured particles is highlighted. Calculation demonstrates that regardless of the degree of ordering, oblate particles (platelets) favor microstructural polarization losses, i.e., the Bruggeman exponent greatly increases. In contrast, prolate particles with very high aspect ratios (needles or fibers) and a great degree of alignment will decrease the α value. (For interpretation of the references to colour in this figure legend, the reader is referred to the web version of this article.)

approximated as a distribution of ellipsoids of rotation, the principal axes are $a = b \neq c$, and the eccentricity is defined as $r_a = c/a = c/b$. Here, the depolarization factors are calculated analytically as reported by Stratton, Torquato, and others [19,21,22]:

$$L = L_x = L_y = \frac{r_a}{2}\int_0^\infty \frac{d\xi}{(\xi + 1)^2\left(\xi + r_a^2\right)^{1/2}}d\xi$$

$$= \begin{cases} \dfrac{r_a}{2}\left(\dfrac{r_a}{r_a^2 - 1} - \dfrac{\text{arcosh}(r_a)}{\left(r_a^2 - 1\right)^{3/2}}\right) & \text{if } r_a > 1 \\[3mm] \dfrac{r_a}{2}\left(\dfrac{r_a}{r_a^2 - 1} + \dfrac{\arccos(r_a)}{\left(1 - r_a^2\right)^{3/2}}\right) & \text{if } r_a < 1 \end{cases}$$ (19)

and

$$L_z = \frac{r_a}{2}\int_0^\infty \frac{d\xi}{(\xi + 1)^2\left(\xi + r_a^2\right)^{3/2}}d\xi$$

$$= \begin{cases} \dfrac{1}{1 - r_a^2} + \dfrac{r_a\,\text{arcosh}(r_a)}{\left(r_a^2 - 1\right)^{3/2}} & \text{if } r_a > 1 \\[3mm] \dfrac{1}{1 - r_a^2} - \dfrac{r_a\arccos(r_a)}{\left(1 - r_a^2\right)^{3/2}} & \text{if } r_a < 1 \end{cases}$$ (20)

where the condition, $L_x + L_y + L_z = 1$ or equivalently, $2L_x + L_z = 1$

must be satisfied. Fig. 3 graphically summarizes Equations 19 and 20 as a function of aspect ratio, r_a.

Define the orientation distribution function of a set of morphologically anisotropic particles in a porous solid, as $P_O = P_O(\vec{t}, \theta, \beta, \gamma)$. Set θ as the cone-angle between the laboratory reference system textured axis, (n_1, n_2, n_3), e.g., along the through-thickness direction, and the textured principal direction, i.e., the c-axis. β is the polar coordinate, and γ is a rotation of the textured axis around itself, in agreement with Bunge [26]. Because the orientation of ellipsoidal particles are insensitive to γ, $P_O(\vec{t}, \theta, \beta, \gamma) \sim P_O(\vec{t}, \theta, \beta)$. While an arbitrarily textured granular solid produces fiber an polar texture contributions, the average fiber contributions correspond to:

$$P_O(\vec{t}, \alpha) = \frac{1}{2\pi} \int_{-\pi}^{\pi} P_T(\vec{t}, \theta, \beta) d\beta \qquad (21)$$

as readily described by Dollase [27]. Therefore, $P_O(\vec{t}, \theta)$ is the probability of finding the textured principal axis at a particular angle with respect to the fiber axis between θ and $\theta + d\theta$. A widely used fiber-texture function is the March-Dollase orientation distribution [27]:

$$\begin{aligned} P_O(t = r, \theta) &= f(r, \theta)\sin\theta \\ &= \frac{\sin\theta}{\left(r^2\cos^2\theta + \frac{1}{r}\sin^2\theta\right)^{3/2}} \end{aligned} \qquad (22)$$

θ typically ranges from 0 and 90°. Values of r range from 0 to 1. A limiting value of $r = 0$ indicates perfect texture, i.e., all the particles are perfectly aligned with the fiber axis. A value of $r = 1$ signifies complete morphological randomness (no texture). Formally, the probability of finding a particle of active material or a grain at a specified orientation in a porous electrode that displays a certain degree of alignment, wi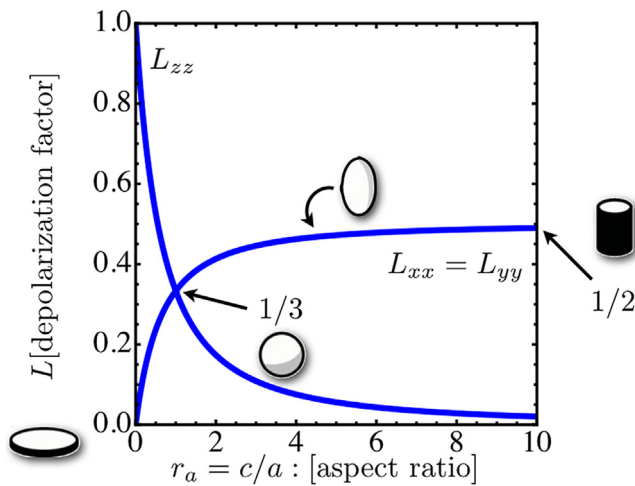th respect to the probability of finding the same orientation in a porous electrode whose particles display a perfectly random orientation distribution defines the Multiples of Random Distribution, MRD [28,29]. In this context, an equivalent definition of the parameterizing value, r, is made in terms of MRD, by setting $MRD = P_O(r, \theta)/P_O(r = 1, \theta) = 1/r^3$, in the limit of $\theta = 0$, as defined more than a decade ago by Fuller et al. [28,29]. Thus, direct substitution into Equation (13) provides a closed expression to the ordering parameter, S:

$$S = \frac{2 + MRD - 3\sqrt{\frac{MRD}{MRD-1}} \, \text{arcosh}\left(\sqrt{MRD}\right)}{MRD - 1} \qquad (23)$$

Equation (23) is graphically depicted in Fig. 4, and shows that a 50% of ordering will develop for $MRD \sim 5$, i.e., there is five times more likelihood to sample an aligned particle than in a perfectly random sample. However, in order to increase the degree of microstructural ordering to 90% its full value, particle alignment must increase to $MRD \sim 40$, an amount of texturing that is experimentally very difficult to accomplish.

Direct substitution of Equations (19) and (23) into Equation (16), for $p = 1$ is graphically summarized in Fig. 5. Results show that in the limit of a perfectly random distribution of particles (no alignment), the lowest tortuosity will be displayed by particles that are perfectly spherical (morphologically isotropic particles). Furthermore, small deviations from perfectly spherical particles will lead to an increase in the Bruggeman exponent, and thus on the through-thickness tortuosity. In the limit of high aspect ratios, prolate particles deliver an asymptotic exponent value of $\alpha \to 2/3$, which in practical systems is virtually indistinguishable from the classic Bruggeman exponent value, $\alpha = 1/2$. In contrast, the fabrication of porous electrodes with oblate particles with a high aspect ratio will deliver very high values of through-thickness tortuosity.

A weak degree of particle alignment, e.g., $MRD \sim 2$, will make the through-thickness tortuosity independent of the morphological anisotropy for prolate-shaped particles, leading to an asymptotic value of $\alpha \sim 1/2$. A strong degree of particle alignment, e.g., $MRD \geq 20$ will lead to $\alpha \leq 1/5$, for a particle anisotropy of $r_a = c/a \geq 4$. In all cases, as compared to randomly oriented particles, any degree of ordering marginally decreases the Bruggeman exponent for oblate
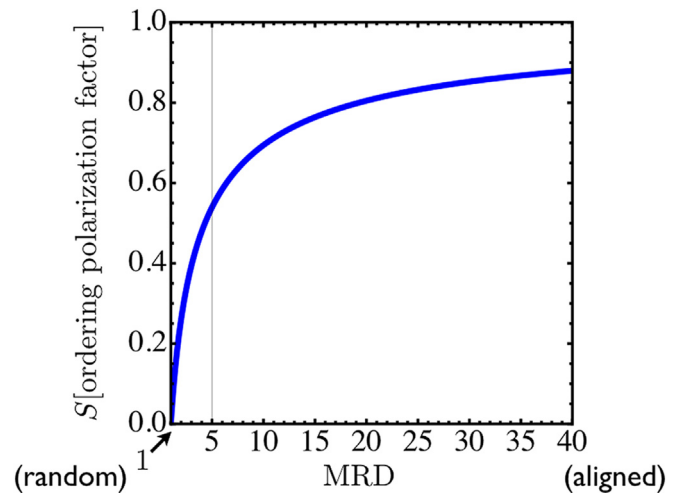

Fig. 3. Depolarization factor for particles comprised of ellipsoids of revolution, of principal axes $a = b$, and c, and anisotropy ratio, $r_a = c/a = c/b$. The depolarization factor reaches its largest value when the surfaces with the widest cross-section are exposed in the direction of the applied charge flux. In the limit of perfectly spherical particles, $L = 1/3$, thus suggesting that each direction, in the reference frame of the particle, contributes equal amounts to the losses. Overall, the geometrical constrain, $L_x + L_y + L_z = 1$, shows that to a first approximation, the depolarization factor is controlled by the relative morphological anisotropy of each particle, not its absolute physical dimensions.

Fig. 4. Microstructural order parameter, S, for a fiber-textured particle orientation distribution, as described by March and later Dollase [27]. S is described in terms of Multiples of Random Distribution, MRD, which highlights the likelihood of identifying an aligned particle in a partially textured sample with respect to a completely untextured sample.
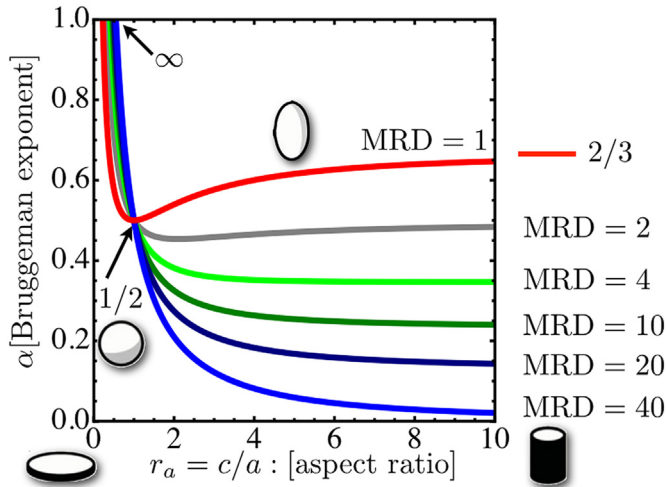
Fig. 5. Bruggeman exponent as a function of particle aspect ratio for different degrees of particle alignment. In the limit of no alignment (complete randomness), the through-thickness Bruggeman exponent $\alpha \to 2/3$, as the shape of the particles become increasingly prolate (needle of fiber-like). A weak degree of particle alignment, *e.g.*, $MRD \sim 2$, simply makes the Bruggeman exponent insensitive to particle morphology, $\alpha \sim 0.45$. A great degree of prolate particle alignment throughout the thickness of the electrode, $MRD \geq 40$, will favor very low Bruggeman exponents. In all cases, $\alpha \to \infty$, for oblate particles (platelets), as $r_a \to 0$, and $\alpha = 1/2$, for perfectly spherical particles, $r_a = 1$, as readily known in the literature.

particles whose c-axis possess a greater than random chance to be aligned along the through-thickness direction; however, the overall effect is to drastically increase it. An alternate graphical depiction of the effect of texture on the through-thickness Bruggeman exponent can be found in the Appendix.

Application of this description to experimentally fabricated electrodes is shown in Table 1, which summarizes a direct comparison between the developed analytical model, a Finite Element calculation that uses three-dimensionally reconstructed porous electrode microstructures for different degrees of morphological anisotropy, as reported by Chung, Ebner et al. [10], and against a recently published semi-analytical model [16], which also uses two-dimensional CT-sections of the same battery electrodes to estimate the through-thickness tortuosity. Results not only demonstrate that the through-thickness Bruggeman exponent correlates very well with published descriptions, but details the microstructural fundamentals and practical limits behind each particle morphology. In all cases, calculations show great agreement with the numerical and semi-analytical calculations, and allows to infer that the in-plane alignment induced by the electrode compaction during processing leads to *MRD* values ranging from 3 to 8, having a great impact on the through-thickness tortuosity.

While the numerical calculation and the semi-analytical models enable the through thickness computation of the Bruggeman exponent, existing approaches are limited by the availability of three-dimensional tomographic data, thus do not allow to

systematically explore the space of parameters that can be experimentally accessed [10,16]. Moreover, numerical results based on such techniques will always be limited by the availability of computational resources and the physical size of each experimentally reconstructed three-dimensional section. In addition, it has been recognized that the reported semi-analytical method is unable to describe the tortuosity for fiber- and lamella-based structures [16]. In contrast, the description provided in Section 2 and Equation (16) is not limited by the specific morphology of individual particles, but by the possibility of analytically representing complex particle morphologies, and by the mathematical complexities to extending this technique to include clustering and other non-idealities present in emerging battery formulations.

A direct extension to describe commercial batteries comprised of a mixture of two types of particles, *e.g.*, the active material phase and the conductive mesoparticle phase, each of them with their specific tortuosity, or the possibility of including the effect particle size and porosity gradients can be readily incorporated in this description by following the formulation of Vijayaraghavan et al. [15]. Here, the total tortuosity of the combined system is given by $\tau_T = \tau \times \tau_\nu$. Thus, the microstructure with the highest degree of morphological anisotropy will enhance the total tortuosity of the composite electrode.

The optimal battery microstructure would not only deliver a minimal amount of microstructural polarization losses but the largest possible delivered instantaneous power density, which in the absence of transport limitations is directly a result of the interfacial area density available for de/intercalation. For particle morphologies that differ from the spherical ideal, and following the analysis that lead to Equations (3) and (4), a more realistic description of the reactive area density includes the particle size anisotropy by analytically computing the area and volume of a representative ellipsoidal particle, immersed in a porosity, ε:

$$\mathscr{A} = \frac{3(1-\varepsilon)}{2r_a r_p} \left(1 + r_a^2 \frac{\arctan\left[\sqrt{r_a^2 - 1}\right]}{\sqrt{r_a^2 - 1}} \right) \tag{24}$$

Equation (24) is graphically summarized in Fig. 6, and reduces to Equation (3) in the limit of $r_a = 1$ (perfect spheres). Calculations show that in the limit of a porous electrode comprised of fiber-based particles, *i.e.*, $r_a \to \infty$, the functional form of the reactivity asymptotically converges to $\mathscr{A} = 3\pi(1-\varepsilon)/4r_p$, which decreases the reactive area per unit volume by $\sim 24\%$, with respect to a distribution of perfectly spherical particles. In contrast, the area per unit volume of oblate particles increases without bounds, as r_a decreases. This strongly suggests that prolate particles deliver the largest instantaneous power density, being only constrained by the transport limitations and microstructural polarization losses, as described by Equation (14).

4. Summary and conclusions

The present work provides the fundamental basis to quantify the microstructural contributions to the transport properties in

Table 1
Bruggeman exponents for different porous materials, as reported by numerical [10], and semi-analytical [16] calculations. Published results are compared against Equation (16). For graphite, Equation (16) was computed by using $MRD = 3.55$, $r_a = 1/5$; for LCO, $MRD = 5$, and $r_a = 1/2$; and for NMC, $MRD = 8$, $r_a = 8/9$. Aspect ratio and degree of alignment were inferred by using data reported by Ebner and Chung [10].

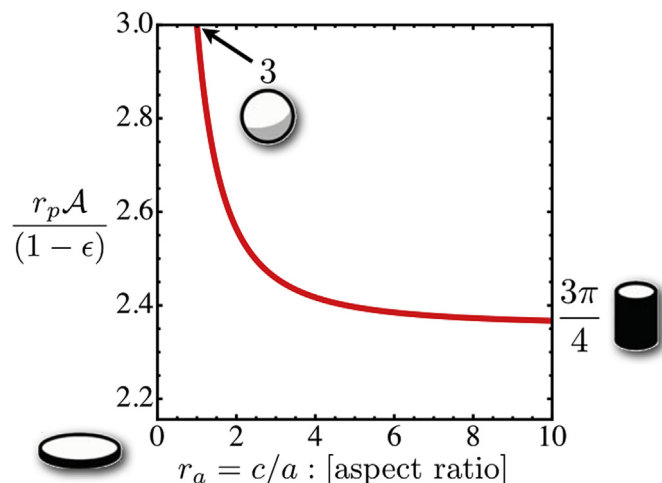| Material	Numerical Bruggeman exponent [10]	Semi-analytical Bruggeman exponent [16]	Analytical Bruggeman exponent (this work)
LCO	0.83	0.78	0.868
NMC	0.57	0.53	0.55
Graphite	1.949	2.08	1.947

Fig. 6. Normalized reactive area density, $\mathscr{A}$, for a porous electrode comprised of a random distribution of ellipsoidal of revolution particles of active material as a function of particle aspect ratio, $r_a = c/a$. Results show that the reactive area density drops by $\sim 24\%$ for prolate particles of very high aspect ratio, and can be maximized for oblate particles (platelets or lamella) of very high aspect ratios.

porous materials comprised of powders of a specified particle size and shape distribution, including its polydispersity throughout the thickness of the electrode layer. By starting from the description of the fields inside an arbitrarily shaped particle, we developed a formalism that allows to analytically compute the Bruggeman exponent and correlate its value to the utilized materials and electrode processing.

As an application, we showed that for ellipsoidal-shaped particles, the effect of morphological anisotropy, electrode layer thickness and the alignment of the starting powders plays a critical role in specifying the through-thickness macroscopic response of these technologically relevant systems. Moreover, microstructural polarization losses and reactive area density define tradeoffs that enable the selection of prolate particles for high energy density applications, and oblate particles for high power density systems, for electrodes that primarily cycle along the through-thickness direction. As readily reported in the literature, and as formulated herein, the in-plane tortuosity is expected to decrease as the through-thickness tortuosity increases [10,16]. The tradeoff between reaching maximal reactivity density and minimal through-thickness tortuosity suggests that for a specified representative particle morphology and power density application a unique porosity value exists that optimizes the power and energy density of the electrode. For textured (aligned) porous electrodes, the optimal microstructure will be found in the limit of very low porosities for fiber-shaped particle morphologies, and for very high porosities in the case of platelet-like architectures. For untextured (no particle alignment), the present analysis suggests that perfectly spherical particles will provide the highest energy densities. Textured, prolate-shaped particles will deliver a morphology independent performance, and its energy density will only be limited by the maximum amount of fibers that can be packed.

While current battery architectures have favored the fabrication of platelet-based porous electrode architectures (*e.g.*, LFP- and graphite-based systems), the present paper provides a context for the selection of powder morphologies, porosities, and its processing for the identification of parameters that will lead to microstructures of improved performance for both though-thickness and in-plane directions. In combination with

the extensive body of work on porous electrode theory and its applications to the modeling and simulation of time-dependent transport of rechargeable batteries, *e.g.*, Refs. [17,18], the microstructural polarization contributions can be quantified and then minimized with the analytical framework presented herein. For example, the threshold current density that leads to severe microstructurally induced polarization losses can be quantified, and by using microstructurally averaged descriptions, such as those proposed by Bazant and coworkers [32], the effect of microstructure on battery materials displaying C-rate dependent two-phase (or full solid solution solubility) can be engineered.
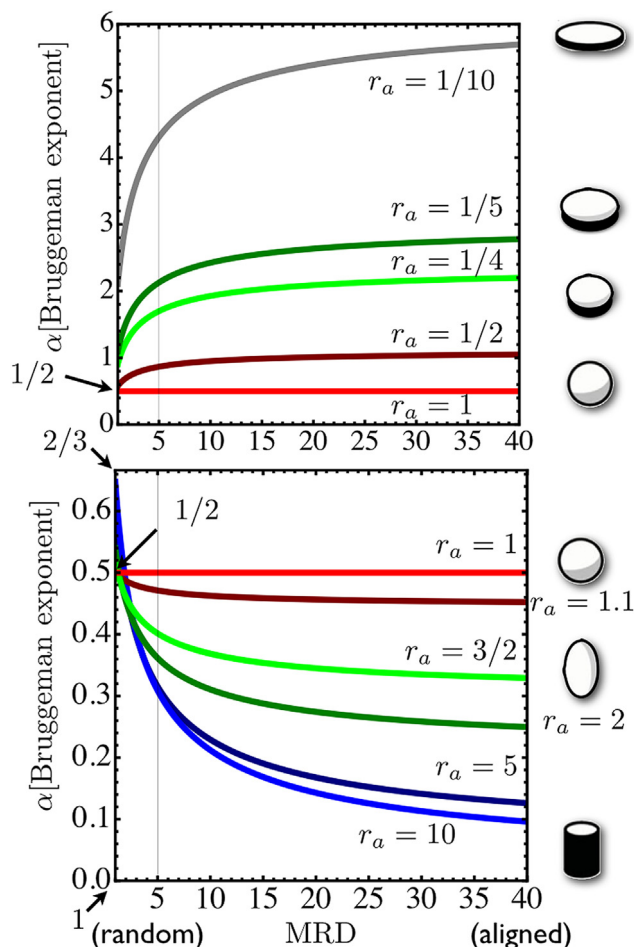
5 Acknowledgments

Appendix

Fig. 7. Bruggeman exponent as a function of the degree of fiber texture for different degrees of particle aspect ratio. Top inset shows oblate-shaped particles (platelets), and bottom inset shows prolate-shaped particles (rods). For oblate-shaped particles (platelets), a weak degree of alignment will greatly increase the Bruggeman exponent $\alpha \sim 6$ for $r_a = 1/10$. Rod-like structures require a great deal of alignment to deliver a Bruggeman exponent significantly lower than that delivered by perfectly spherical particles.

References

[1] J.M. Tarascon, M. Armand, Issues and challenges facing rechargeable lithium batteries, Nature 414 (2001) 359–367.

[2] M.S. Whittingham, Materials challenges facing electrical energy storage, MRS Bull. 33 (2008) 411–420.

[3] T. Marks, S. Trussler, A.J. Smith, D. Xiong, J.R. Dahn, A guide to Li-Ion coin-cell electrode making for academic researchers, J. Electrochem. Soc. 158, (1) (2011) A51–A57.

[4] C.M. Doyle, Design and Simulation of Lithium Rechargeable Batteries, PhD thesis, University of California at Berkeley, Berkeley, CA, 1995.

[5] D.A. Bruggemann, Berechnung verschiedener physicalischer konstate von heterogen substanzen, Ann. Phys. 24 (1935) 636–664.

[6] I.V. Thorat, D.E. Stephenson, N.A. Zacharias, K. Zaghib, J.N. Harb, D.R. Wheeler, Quantifying tortuosity in porous Li-ion battery materials, J. Power Sources 188 (3) (2009) 592–600.

[7] P.R. Shearing, L.E. Howard, P.S. Jorgensen, N.P. Brandon, S.J. Harris, Characterization of the 3-dimensional microstructure of a graphite negative electrode from a Li-ion battery, Electrochem. Commun. 12 (2010) 374–377.

[8] D.-W. Chung, M. Ebner, D.R. Ely, V. Wood, R.E. García, Validity of the Bruggeman relation for porous electrodes, Model. Simul. Mater. Sci. Eng. 21 (7) (2013) 064009.

[9] D.-W. Chung, P.R. Shearing, N.P. Brandon, S.J. Harris, R.E. García, Particle size polydispersity in Li-ion batteries, J. Electrochem. Soc. 161 (3) (2014) A422–A430.

[10] M. Ebner, D.-W. Chung, R.E. García, V. Wood, Tortuosity anisotropy in lithium-ion battery electrodes, Adv. Energy Mater. 4 (5) (2014) 1301278.

[11] L. Shen, Z. Chen, Critical review of the impact of tortuosity on diffusion, Chem. Eng. Sci. 62 (2007) 3748–3755.

[12] I. Srivastava, S. Sadasivam, K.C. Smith, T.S. Fisher, Combined microstructure and heat conduction modeling of heterogeneous interfaces and materials, J. Heat Transf. 135 (6) (2013) 061603.

[13] M. Smith, Q.C. Horn, R.E. García, The effect of microstructure on the galvanostatic discharge of graphite anode electrodes in LiCoO^2-based rocking chair rechargeable batteries, J. Electrochem. Soc. 156 (2009) A896–A904.

[14] B. Vijayaraghavan, R.E. García, Y.-M. Chiang, Microstructure Modeling of Rechargeable Lithium-ion Batteries, 219th ECS Meeting, MA2011–01, Canada, B5-Microstructure, Mechanisms, and Modeling of Battery Materials, Montreal, QC, May 1–May 6, 2011.

[15] B. Vijayaraghavan, D.R. Ely, Y.-M. Chiang, R. García-García, R.E. García, An analytical method to determine tortuosity in rechargeable battery electrodes, J. Electrochem. Soc. 159 (9) (2012) A548–A552.

[16] M. Ebner, V. Wood, Tool for tortuosity estimation in lithium ion battery porous electrodes, J. Electrochem. Soc. 162 (2) (2015) A3064–A3070.

[17] M. Doyle, J. Newman, A.S. Gozdz, N. Schmutz, J.-M. Tarascon, Comparison of modeling predictions with experimental data from plastic lithium ion cells, J. Electrochem. Soc. 143 (1996) 1890–1903.

[18] T.F. Fuller, M. Doyle, J. Newman, Simulation and optimization of the dual lithium-ion insertion cell, J. Electrochem. Soc. 141 (1) (1994).

[19] S. Giordano, Effective medium theory for dispersions of dielectric ellipsoids, J. Electrost. 58 (2003) 59–76.

[20] S. Giordano, Order and disorder in heterogeneous material microstructure: Electric and elastic characterisation of dispersions of pseudo-oriented spheroids, Int. J. Eng. Sci. 43 (2005) 1033–1058.

[21] S. Torquato, Random Heterogeneous Materials: Microstructure and Macroscopic Properties." Interdisciplinary Applied Mathematics v. 16, Springer Science & Business Media, 2013, 703 pages.

[22] J.A. Stratton, Electromagnetic Theory, John Wiley & Sons, Jan 22, 2007, 615 pages.

[23] A. Donev, I. Cisse, D. Sachs, E.A. Variano, F.H. Stillinger, R. Connelly, S. Torquato, P.M. Chaikin, Improving the density of jammed disordered packings using ellipsoids, Science 303 (2004) 990–993.

[24] W. Lai, C.K. Erdonmez, T.F. Marinis, C.K. Bjune, N.J. Dudney, F. Xu, R. Wartena, Y.-M. Chiang, Ultrahigh-energy-density microbatteries enabled by new electrode architecture and micropackaging design, Adv. Mater. 22 (2010) E139–E144.

[25] C.-J. Bae, C.K. Erdonmez, J.W. Halloran, Y.-M. Chiang, Design of battery electrodes with dual-scale porosity to minimize tortuosity and maximize performance, Adv. Mater. 25 (2013) 1254–1258.

[26] H.-J. Bunge, Texture Analysis in Materials Science, Butterworths, London, 1993.

[27] W.A. Dollase, Correction of intensities for preferred orientation in powder diffractometry: application of the March model, J. Appl. Crystallogr. 19 (1986) 267–272.

[28] M.M. Seabaugh, M.D. Vaudin, J.P. Cline, G.L. Messing, Comparison of Texture Analysis Techniques for Highly Oriented α-Al$_2$O$_3$, J. Am. Ceram. Soc. 83 (8) (2000) 2049–2054.

[29] J.E. Blendell, M.D. Vaudin, E.R. Fuller Jr., Determination of texture from individual grain orientation measurements, J. Am. Ceram. Soc. 82 (11) (1999) 3217–3220.

[32] T.R. Ferguson, M.Z. Bazant, Nonequilibrium thermodynamics of porous electrodes, J. Electrochem. Soc. 159 (12) (2012) A1967–A1985.